The Astrophysical Journal, 622:1202–1210, 2005 April 1

A FULL VIEW OF EIT WAVES

P. F. Chen,[1] C. Fang,[1] and K. Shibata[2]

Received 2004 August 2; accepted 2004 December 8

ABSTRACT

Early observations by the EUV Imaging Telescope (EIT) on the *Solar and Heliospheric Observatory* indicated that propagating diffuse wave fronts, now conventionally referred to as "EIT waves," can often be seen on the solar disk with a propagation velocity several times smaller than that of Hα Moreton waves. They are almost always associated with coronal mass ejections. We have previously confirmed the existence of such a wave phenomenon with numerical simulations, which indicate that there does exist a slower moving "wave" much behind the coronal counterpart of the Hα Moreton wave. Further observations have disclosed many new features of the EIT waves: the waves stop near the separatrix between active regions, sometimes they experience acceleration from the active region to the quiet region, and so on. Here we report on MHD simulations performed to demonstrate how the typical features of EIT waves can all be accounted for within our theoretical model, in which the EIT waves are thought to be formed by successive stretching or opening of closed field lines driven by an erupting flux rope. The relationship between EIT waves, Hα Moreton waves, and type II radio bursts is discussed, with an emphasis on reconciling the discrepancies among different views of the "EIT wave" phenomenon.

Subject headings: Sun: activity — Sun: corona — Sun: magnetic fields — waves

Online material: color figures

1. INTRODUCTION

Since launch in 1995 December, the EUV Imaging Telescope (EIT; Delaboudinière et al. 1995) on board the *Solar and Heliospheric Observatory* (*SOHO*) has revealed many new observational features of the solar corona in the 1–2 MK temperature range, such as intermingling of cool and hot coronal loops, intensity oscillations in the transition region and corona, and extreme-ultraviolet (EUV) jets in the dynamic coronal hole (Moses et al. 1997). Among these, one spectacular phenomenon, conventionally referred to as "EIT waves," not only manifests the signature of on-disk coronal mass ejections (CMEs) in the low corona but has also sparked hot debate on the relation between EIT waves and Moreton waves, which were discovered about 40 years ago.

When the magnetic structure on the solar surface is simple, EIT waves are observed as almost circularly propagating, diffuse emission enhancements immediately followed by expanding "dimming regions" in *SOHO* EIT running-difference images (Moses et al. 1997; Thompson et al. 1998). When the global magnetic structure becomes complicated, EIT waves instead propagate inhomogeneously, avoiding strong magnetic features and neutral lines and stopping near coronal holes (Thompson et al. 1999). They may also stop near the separatrix between active regions and thus appear as a stationary front (Delannée & Aulanier 1999). Limb events have also been reported, in which the "EIT wave" front is found to surround a dark cavity in the *SOHO* EIT running-difference images (Dere et al. 1997). A statistical study by Klassen et al. (2000) indicates that the typical velocities of EIT waves range from 170 to 350 km s^{-1} with an average of 271 km s^{-1}, and velocities as low as 80 km s^{-1} have occasionally been reported (Dere et al. 1997). EIT waves can also be observed by the *Transition Region and Coronal Explorer* (*TRACE*) in the same 195 Å passband (Wills-Davey & Thompson 1999).

The discovery of one sharp EUV wave front cospatial with an Hα Moreton wave front in a flare event on 1997 September 24 made it natural to explain the observed EIT waves as being just the coronal counterparts of the chromospheric Moreton waves—that is, coronal fast-mode waves (see, e.g., Thompson et al. 2000). Similar events, with a sharp EUV wave front cospatial with a corresponding Hα Moreton wave front, have also been presented by Warmuth et al. (2004a). On the other hand, there are also many events in which a sharp EUV wave front is seen to be cospatial with a soft X-ray (SXR) wave front, the latter of which exhibits the characteristics of coronal fast-mode waves (or weak shock waves; see, e.g., Khan & Aurass 2002; Hudson et al. 2003). All these results tend to favor the coronal fast-mode wave model for EIT waves. The hypothesis was tested in model simulations by Wang (2000), who illustrated that the ray paths of fast-mode waves can match the EIT bright fronts. In particular, it was found that the waves are deflected away from active regions and coronal holes, reproducing the observed tendency of EIT waves to avoid strong magnetic features and to stop near coronal holes. Wu et al. (2001) performed three-dimensional numerical simulations of the perturbation that is induced by a pressure pulse localized in the source region of a CME. They found that the resulting fast-mode wave fronts in the corona reproduce many properties of the observed EIT waves. We note that both Wang (2000) and Wu et al. (2001) used large-scale magnetograms from the Wilcox Solar Observatory to extrapolate the coronal magnetic field. The averaged weak magnetic field, along with the adopted density model, results in a plasma β higher than unity in the quiet region, where most EIT waves are observed. Such a high β is probably unrealistic in the lower corona and is not consistent with the potential or force-free assumption for the coronal field extrapolation.

The obvious defect of the fast-mode wave explanation is that the velocities of EIT waves, 170–350 km s^{-1} as reported by Klassen et al. (2000), are about a third or less of those of Moreton waves, which range from 330 to 4200 km s^{-1} as measured through Hα images and inferred from the "winking" of

[1] Department of Astronomy, Nanjing University, 210093 Nanjing, China; chenpf@nju.edu.cn.
[2] Kwasan Observatory, Kyoto University, Kyoto 607-8471, Japan.

remote filaments (Smith & Harvey 1971). This large velocity discrepancy between the two phenomena was later explained by Warmuth et al. (2001, 2004b) as being due to the deceleration of the waves, though the winking of remote filaments does not imply the deceleration of Moreton waves, and Foley et al. (2003) found in one event that the EIT wave velocity near the source active region was ~80–120 km s^{-1}, which is smaller than that in the quiet region observed later and even smaller than the sound speed in the low corona. Moreover, Harra & Sterling (2003) found with *TRACE* data that not far from the flare site, the speed of the EIT waves (in the conventional sense) is only ~200 km s^{-1}, less than half that of a preceding wave, in which case the faster wave could correspond to a coronal Moreton wave.

The occasional occurrence of stationary EIT wave fronts led Delannée & Aulanier (1999) and Delannée (2000) to doubt the magnetoacoustic-wave explanation for EIT waves. They were the first to link EIT waves to the magnetic field evolution involved in CMEs. They suggested that the EIT bright front is halted to form a stationary front when it encounters regions where the magnetic field is more or less vertical (e.g., a separatrix). We performed MHD numerical simulation of CMEs (Chen et al. 2002) and found two associated wavelike patterns: a piston-driven shock is formed straddling the erupting flux rope, which sweeps the solar surface at a super-Alfvénic velocity; simultaneously, a slower moving wavelike structure, with enhanced density bordering an expanding dimming region, is discerned to move with a velocity about one-third that of the fast wave. We proposed that the top of the piston-driven shock corresponds to the source of type II radio bursts, while its skirt is the coronal counterpart of Hα Moreton waves (or coronal Moreton waves), and the slower moving wavelike structure corresponds to the EIT waves, which are formed by successive opening of the field lines covering the erupting flux rope rather than being a real wave. This model was later confirmed by Harra & Sterling (2003) and Foley et al. (2003). The former found that two waves with different speeds are associated with a CME event.

In this paper, we present further numerical simulations in order to clarify the debate over the nature of EIT waves and provide explanations for the sharp EIT wave front occasionally seen to be cospatial with Hα Moreton waves, the stationary EIT wave front, and the acceleration of the EIT waves. In § 2, the numerical method is described. Numerical results are presented in § 3. We conclude by discussing the application of our model to the aforementioned features in § 4.

2. NUMERICAL METHOD

We use an implicit multistep scheme (Hu 1989; further developed in Chen et al. 2000) to numerically solve the following two-dimensional, time-dependent, compressible resistive MHD equations in Cartesian coordinates:

$$\frac{\partial \rho}{\partial t} + \nabla \cdot (\rho \boldsymbol{v}) = 0, \tag{1}$$

$$\frac{\partial \boldsymbol{v}}{\partial t} + (\boldsymbol{v} \cdot \nabla)\boldsymbol{v} + \frac{\nabla P}{\rho} - \frac{1}{\rho}(\nabla \times \boldsymbol{B}) \times \boldsymbol{B} - \boldsymbol{F} = 0, \tag{2}$$

$$\frac{\partial \psi}{\partial t} + \boldsymbol{v} \cdot \nabla \psi - \eta \, \Delta \psi = 0, \tag{3}$$

$$\frac{\partial T}{\partial t} + \boldsymbol{v} \cdot \nabla T + (\gamma - 1) T \nabla \cdot \boldsymbol{v} - \frac{2(\gamma - 1)\eta}{\rho \beta} (\nabla \times \boldsymbol{B})^2 = 0, \tag{4}$$

where $\gamma = 5/3$ is the ratio of specific heats, $\boldsymbol{F}$ is an external force keeping the initial configuration in equilibrium and driving the flux rope to erupt, and η is the dimensionless resistivity, that is, the inverse of the magnetic Reynolds number. For simplicity, gravity is omitted. The five independent variables are the density (ρ), velocity (v_x, v_y), magnetic flux function (ψ), and temperature (T); note that the magnetic field $\boldsymbol{B}$ is related to the magnetic flux function through $\boldsymbol{B} = \nabla \times (\psi \hat{\boldsymbol{e}}_z)$. The equations are nondimensionalized using the following characteristic values: $\rho_0 = 1.67 \times 10^{-13}$ kg m^{-3}, $T_0 = 1.5 \times 10^6$ K, $L_0 = 2 \times 10^4$ km, and $\beta = 0.15$, where β is the plasma beta at the point (0, 4.9) in the dimensionless coordinates (note that the dynamic quantities, such as the velocity, in the results are independent of ρ_0 and L_0). So, the characteristic Alfvén speed is 575 km s^{-1} and the Alfvén timescale is $\tau_A = 35$ s. The dimensionless resistivity η is distributed as

$$\eta = \begin{cases} \eta_0 \cos 1.8\pi x & \text{if } |x| \le 0.3 \\ \quad \times \cos[(y - y_n)\pi], & \text{and } |y - y_n| \le 0.5, \\ 0, & \text{elsewhere,} \end{cases} \tag{5}$$

where $\eta_0 = 0.02$ and y_n is the height of the reconnection X-point.

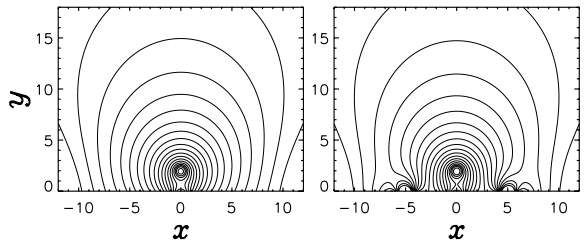

FIG. 1.—Initial magnetic configurations in case A (*left*) and case B (*right*). In case A, the background field is bipolar, while in case B another two active regions reside in the background field.

As pointed out in § 1, EIT wave fronts are almost circular when only one active region is on the disk, while they break into many pieces when the global magnetic field becomes complex. Correspondingly, two types of initial magnetic configurations, denoted cases A and B, are applied in this paper, as shown in Figure 1. In case A, a flux rope is embedded in a dipolar background field, the same as the one used in Chen et al. (2002); that is, the magnetic field consists of a line current (ψ_l), its image current (ψ_i), and the background field (ψ_b), as follows:

$$\psi_l = \begin{cases} \frac{1}{2} r^2 / r_0, & \text{if } r \le r_0, \\ \frac{1}{2} r_0 - r_0 \ln r_0 + r_0 \ln r, & \text{if } r > r_0, \end{cases} \tag{6}$$

$$\psi_i = -\tfrac{1}{2} r_0 \ln[x^2 + (y + 2)^2], \tag{7}$$

$$\psi_b = 0.143 \times \ln \frac{[(x + 0.3)^2 + (y + 0.3)^2][(x - 0.3)^2 + (y + 0.3)^2]}{[(x + 15)^2 + (y + 0.3)^2][(x - 15)^2 + (y + 0.3)^2]}, \tag{8}$$

where $r = [x^2 + (y - 2)^2]^{1/2}$ and $r_0 = 0.5$ is the radius of the flux rope. In case B, two more active regions are placed symmetrically on either side of the source active region. The contribution of the side regions to the background magnetic field is

$$\psi = 0.5 \ln \frac{[(x + 4)^2 + (y + 0.3)^2][(x + 6)^2 + (y + 0.3)^2]}{[(x + 4.8)^2 + (y + 0.3)^2][(x + 5.2)^2 + (y + 0.3)^2]} + 0.5 \ln \frac{[(x - 4)^2 + (y + 0.3)^2][(x - 6)^2 + (y + 0.3)^2]}{[(x - 4.8)^2 + (y + 0.3)^2][(x - 5.2)^2 + (y + 0.3)^2]}. \tag{9}$$

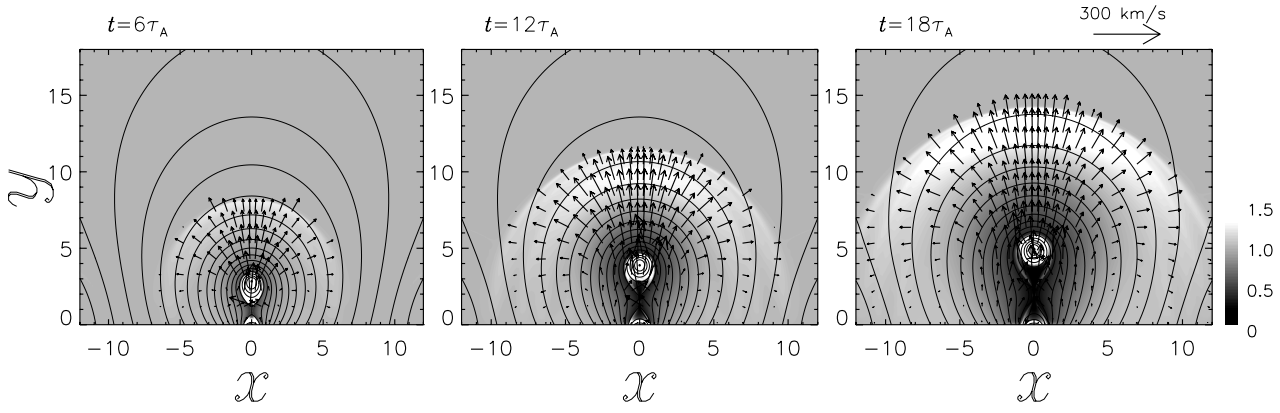

FIG. 2.—Evolution of the density (*gray scale*), magnetic field (*solid lines*), and velocity (*arrows*) in case A. A piston-driven shock straddles the erupting flux rope, with the legs sweeping the solar surface and an expanding dimming region lagging far behind. [*See the electronic edition of the Journal for a color version of this figure.*]

As the initial conditions, a uniform temperature $T = 1$ is assumed and the density is distributed as

$$\rho = \begin{cases} 1 + 2\beta_0^{-1}(1 - r^2/r_0^2), & \text{if } r \le r_0, \\ 1, & \text{if } r > r_0, \end{cases} \tag{10}$$

where β_0 is the plasma beta around the flux rope. As in Forbes (1990) and Chen & Shibata (2000), the initial gas pressure balances the magnetic force within the current filament only when the image current and the background field are absent.

The dimensionless size of the simulation box is described by $|x| \le 12$ and $0 \le y \le 18$. Owing to symmetry, the simulations are made only in the right half-region, which is discretized into 148×541 grid points. The bottom of the simulation area is a line-tying boundary, where all quantities are fixed except for T, which is determined by equivalent extrapolation. The left boundary ($x = 0$) is symmetric, while the other two boundaries are open.

To initiate CMEs, shearing motion, converging motion, and flux emergence are all appropriate (see Chen & Shibata 2000). Here, similar to the case in Chen et al. (2002), an upward external force $\boldsymbol{F} = [1.3 + 5.7(v_{\rm rope} - v_c)/v_{\rm rope}]e^{4(\psi_c - \psi)}\hat{\boldsymbol{e}}_y$ is exerted on the flux rope, that is, the region with $-1.5 \ge \psi \ge \psi_c$, where ψ_c is the value of ψ at the center of the flux rope, v_c is the velocity at the flux rope's center, and $v_{\rm rope}$ is a parameter that controls the final velocity of the flux rope. With the specified external force $\boldsymbol{F}$, the final velocity of the flux rope is around $v_{\rm rope}$ with a weak oscillation.

3. NUMERICAL RESULTS

In case A, in which only the source active region is present, the evolution is the same as described in Chen et al. (2002); that is, the external force drives the flux rope to erupt, the plasma below the flux rope is evacuated rapidly, and the lateral plasma, with frozen-in field lines, is driven inward to form a current sheet near the null point. Reconnection is then induced, which is thought to be crucial for the ejection of the flux rope (e.g., Lin & Forbes 2000; Lin 2004). Below the reconnection X-point, cusp-shaped flare loops are formed as shown in Figure 2, which presents the evolution of the density, magnetic field, and velocity for an adopted $v_{\rm rope} = 100$ km s^{-1}. As reconnection proceeds, the flare loop apparently expands and its two footpoints separate, which is the classical paradigm for two-ribbon flares. Field lines covering the flux rope are pushed to expand in both the upward and the lateral directions. As a result, a piston-driven shock appears straddling the flux rope, the top part of which

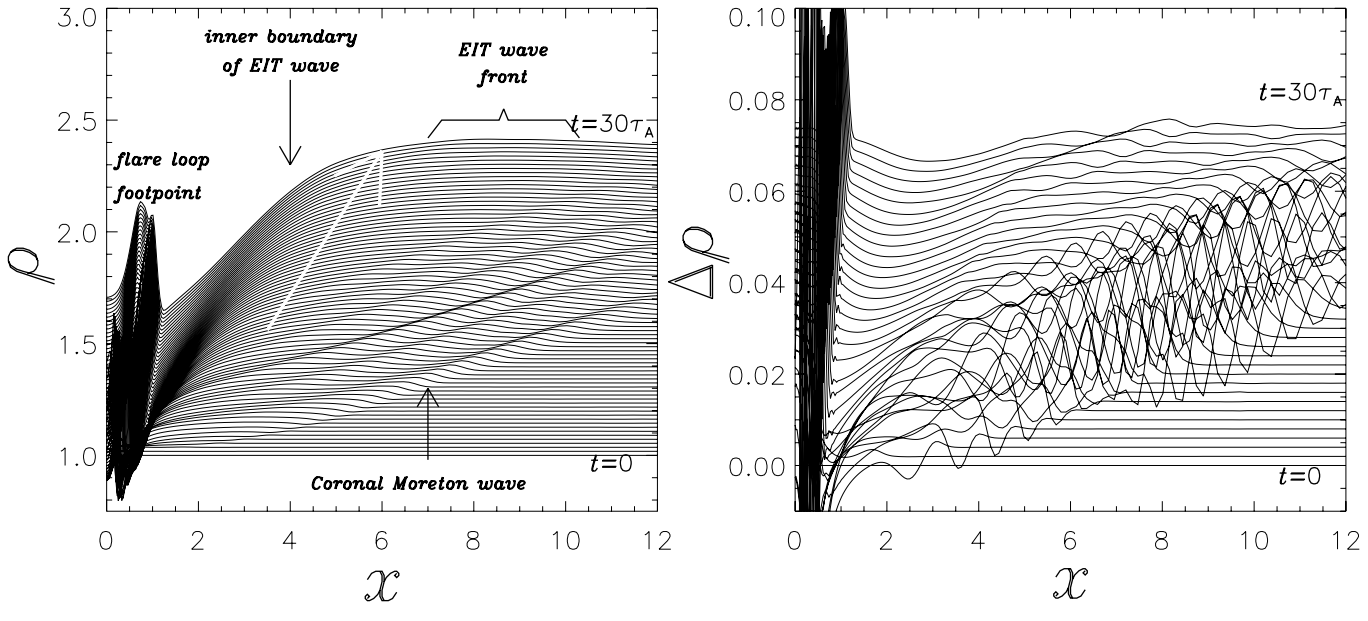

FIG. 3.—Evolution of the density distribution (ρ, *left*) and its running difference ($\Delta\rho$, *right*) along the line $y = 0.5$ for case A. Note that the distribution at each time is stacked on the previous one, with an increment of 0.018 every $0.4\tau_A$ for the left panel and 0.001 every $0.8\tau_A$ for the right panel.

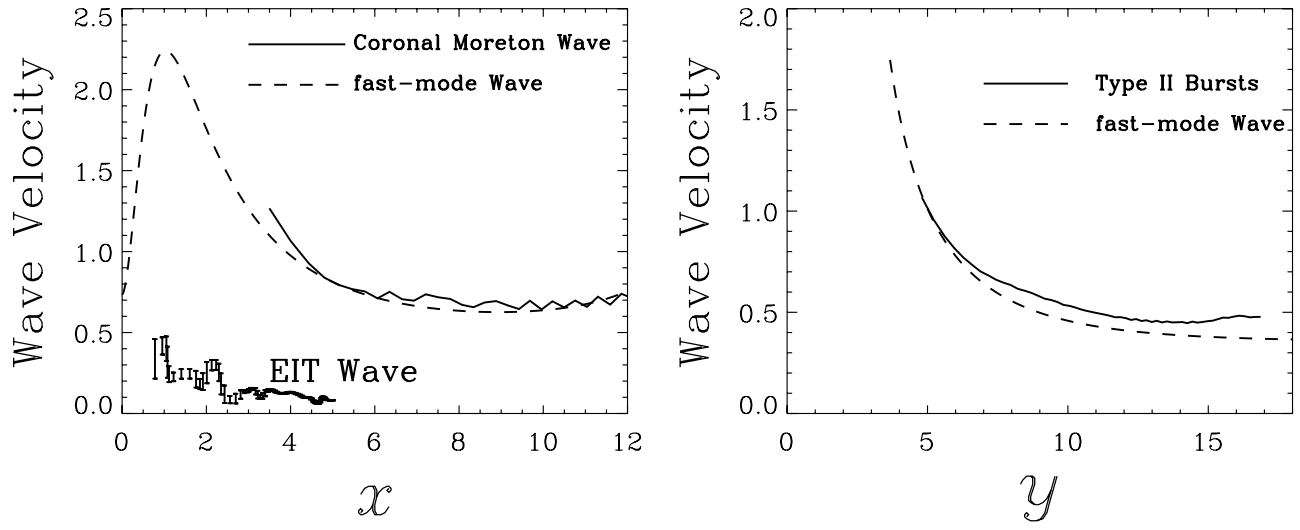

FIG. 4.—*Left*, distribution of the coronal Moreton wave velocity (*solid line*), EIT wave velocity (*error bars*), and local fast-mode wave speed (*dashed line*) along the line $y = 0.5$ in case A; *right*, distribution of the type II burst velocity (*solid line*) and local fast-mode wave speed (*dashed line*) along the y-axis.

moves upward at a speed of 428 km s^{-1} at $y = 7$, larger than the local fast-mode wave velocity; this was interpreted to correspond to the source of type II radio bursts in Chen et al. (2002). Near the bottom boundary, the piston-driven shock may degenerate to a finite-amplitude MHD fast wave, depending on the strength of the shock. On the other hand, a region of depleted density far behind the shock, which may be described as a cavity or a dimming region, is formed surrounding the erupting flux rope and the solar flare.

As time goes on, the skirt of the piston-driven shock sweeps outward rapidly, while the boundary of the dimming region moves much slower. The difference can be seen much more clearly in Figure 3, which depicts the evolution of the density distribution along the right half of the horizontal line $y = 0.5$ in the left panel and the evolution of its running difference in the right panel. In this figure, two wavelike structures are clearly visible besides the motion of the flare loop footpoint. The first wave, which propagates very quickly and lies at the outermost part of the perturbed region, corresponds to the right leg of the piston-driven shock wave and was explained as the coronal counterpart of an Hα Moreton wave (or a coronal Moreton wave) in Chen et al. (2002). It is moving at 398 km s^{-1} when it passes $x = 7$. Between this wave and the flare loop footpoint is the second wavelike structure (*white arrow, left*), which separates a propagating density-enhanced front to the right and an expanding density-depleted region to the left. The nature of this wavelike structure is hinted at by the right panel, where it separates a region full of fast-mode waves on its right side and a quiet region with a smooth $\Delta\rho$ distribution on its left. The propagating density-enhanced front was interpreted as the observed EIT wave in Chen et al. (2002). It moves at 142 ± 4 km s^{-1} averaged from $t = 4\tau_A$ to $t = 10\tau_A$.

The kinematics of the wave phenomena is shown in Figure 4, which displays the distribution of the coronal Moreton wave velocity, the EIT wave velocity, and the local fast-mode wave speed along the line $y = 0.5$ near the surface (*left*) and the distribution of the type II burst velocity and the local fast-mode wave speed along the y-axis (*right*). In the left panel, it can be seen that the fast-mode magnetosonic Mach number of the coronal Moreton wave decreases from 1.15 at $x = 3.5$ to almost unity around $x = 5$. Though there is a slight increase near the weakest magnetic field between $x = 6$ and $x = 9$, possibly owing to nonlinear effects, the Mach number recovers to around unity thereafter. Note that the EIT wave speed is several times smaller than the local fast-mode wave speed. In the right panel, it can be seen that above the erupting flux rope the perturbation steepens into a shock, with the magnetosonic Mach number increasing to $\sim$1.15 between $y = 8$ and $y = 14$. Past $y = 15$, the Mach number even reaches $\sim$1.3. It is straightforward to understand that as the parameter $v_{\rm rope}$ (which controls the final velocity of the flux rope) increases, the piston-driven shock gets stronger, and hence the upward-moving velocity of the top part of the shock increases. We simulated nine cases, with $v_{\rm rope}$ ranging uniformly from 100 to 300 km s^{-1}. In each case, three quantities are calculated: (1) the rising speed of the top part of the piston-driven shock; (2) the horizontal speed of the leg of the piston-driven shock, that is, the coronal Moreton wave; and (3) the EIT wave velocity. Figure 5 plots the variation of the coronal Moreton wave speed and the EIT wave speed versus that of the upward-moving shock. Here we simply assume that the top of the piston-driven shock is the source of type II radio bursts. It can be seen that as the speed of the type II radio source increases, the coronal Moreton wave speed increases

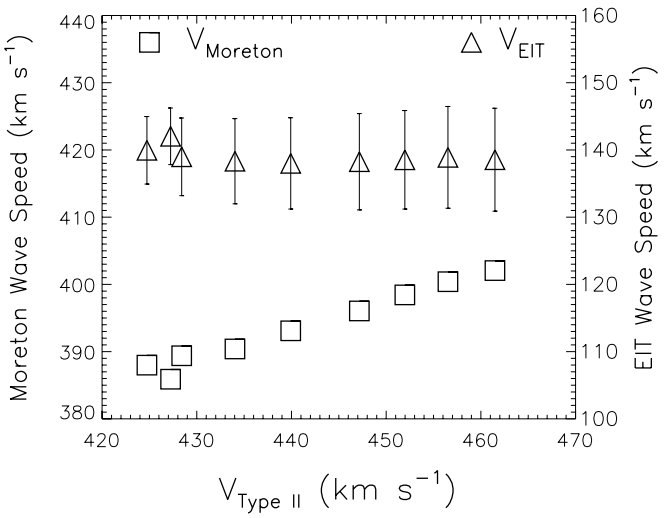

FIG. 5.—Variations of the Moreton wave speed and the EIT wave speed with respect to that of the type II radio source in case A, where the legs of the piston-driven shock are regarded as the coronal Moreton wave and the top part of the piston-driven shock is considered to be the source of type II radio bursts.

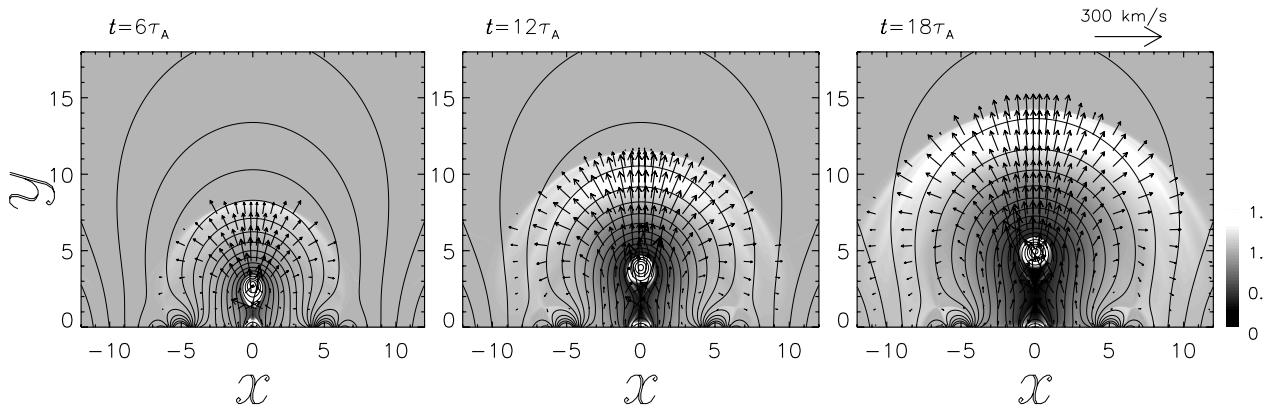

FIG. 6.—Evolution of the density (*gray scale*), magnetic field (*solid lines*), and velocity (*arrows*) in case B. The piston-driven shock is refracted by active regions, and the following EIT wave stops near their boundary. [*See the electronic edition of the Journal for a color version of this figure.*]

correspondingly; the EIT wave speed, however, shows little variation.

In case B, where another two active regions reside symmetrically in the background, the initial evolution is quite similar to that in case A. However, when the coronal Moreton waves reach the side active regions, they are deflected slightly by the strong magnetic field and rapidly circumvent the active regions, as illustrated by Figure 6. Thereafter, the coronal Moreton waves continue to propagate outward. In contrast, when the EIT waves propagate to the boundary of the side active regions, they are halted. This is clearly illustrated by Figure 7, which plots the evolution of the density distribution along the right half of the horizontal line $y = 0.5$, with the density distribution at each time stacked on the previous one with an increment of 0.018 every $0.4\tau_A$. The spectacular difference from case A (see Fig. 3) is that after $t \approx 15\tau_A$, the EIT wave remains stationary at $x \approx 4.5$. Compared with the magnetic configuration of case B (Fig. 1, *right*), it is found that the stationary front is almost cospatial with the local separatrix.

4. DISCUSSION

4.1. *Model of the EIT Waves*

More than 40 years ago, it was found that Hα disturbances in some flare events propagate through the chromosphere over distances on the order of 5×10^5 km with velocities ranging from 500 to 2000 km s^{-1}, which later came to be called Moreton waves (Moreton & Ramsey 1960). These properties could not be accounted for by any wave of chromospheric origin, so they presented quite a puzzle for researchers. Uchida (1968) proposed that the skirt of the wave-front surface of a coronal fast-mode wave sweeps the chromosphere and produces the Moreton waves. The wave is refracted toward a low Alfvén velocity region to sharpen into an enhanced fast-mode shock wave that could emit type II radio bursts in the corona (Uchida 1974). This model is in agreement with the strong relationship between Moreton waves and radio bursts found by Kai (1970), and it confirms the proposal by Wild et al. (1963) that Moreton waves could have the same origin as the type II radio bursts. Therefore, there should be a coronal counterpart to Hα Moreton waves, though the search for such a wave was not so successful until a few years ago (e.g., Khan & Aurass 2002; Hudson et al. 2003). The recent discovery of the EIT waves sparked intense interest in this topic (e.g., Moses et al. 1997; Thompson et al. 1998). Since EIT waves propagate across magnetic field lines in the corona, and their velocities are typically—though not for all events—larger than the sound speed in the low corona (Klassen et al. 2000), they were naturally explained in terms of fast-mode waves, or as the coronal counterparts of chromospheric Moreton waves (e.g., Thompson et al. 1999; Klassen et al. 2000). However, statistical research by Smith & Harvey (1971) and Klassen et al. (2000) has indicated that the velocities of Moreton waves are generally 2–3 or even more times as large as those of EIT waves, which strongly suggests that the two kinds of waves are quite different phenomena.

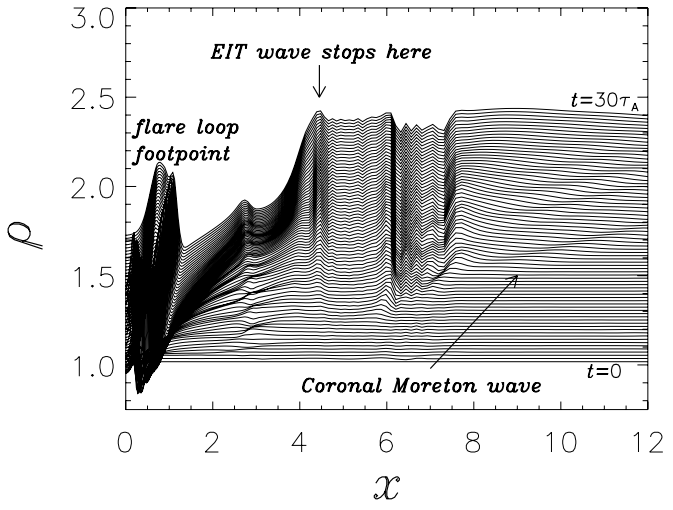

FIG. 7.—Evolution of the density (ρ) distribution along the line $y = 0.5$ for case B, in which another active region is located between $x = 4$ and $x = 6$. Note that the ρ-distribution at each time is stacked on the previous one, with an increment of 0.018 every $0.4\tau_A$.

In order to reconcile the discrepancy, we numerically simulated the wave phenomena induced by CMEs (Chen et al. 2002). It was found that as the flux rope is ejected, field lines covering the flux rope are pushed to expand and a piston-driven shock appears straddling the flux rope, which sweeps the solar surface at a super-Alfvénic speed. This was explained as the coronal counterpart of the chromospheric Moreton waves. Simultaneously, a slower moving wavelike pattern is discerned with an enhanced-density region ahead. The propagating density enhancement was proposed to correspond to the observed EIT waves. For the case $\beta = 0.05$, the speed of the coronal Moreton waves was $\sim$773 km s^{-1}, while that of the EIT waves was $\sim$250 km s^{-1}. The result is consistent with the statistical research (Smith & Harvey 1971; Klassen et al. 2000), as well as a case study by Eto et al. (2002). Based on the analysis of the numerical results, we pointed out that coronal Moreton waves are shock waves driven by CMEs rather than any blast wave

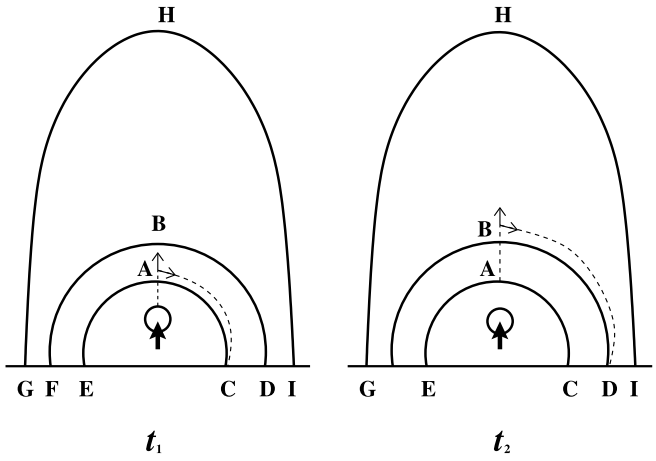

FIG. 8.—Schematic diagram illustrating how the opening-related perturbation induced by the erupting flux rope is transferred from the top to the footpoint of each field line so that EIT wave fronts are formed successively, from point C to point D at two different times. Note that the transfer of the perturbation to the left footpoints of the field lines is not shown here.

directly associated with flares. Most importantly, as suggested by the numerical results, we proposed a theoretical model for the EIT waves; that is, the observed EIT waves are more akin to a propagating wave packet than to waves of any mode, and they are formed by successive stretching (or opening in a general sense) of the field lines, in which the stretching is initiated by the erupting flux rope and is transferred from the top to the footpoint of any individual field line. The model is schematically depicted in Figure 8: As the flux rope rises, the field line near point A is first pushed and stretched. The induced perturbation will propagate out as a piston wave or piston shock, while the large-amplitude deformation itself will be transferred along the field line down to footpoint C (as well as E) by Alfvén waves and also across the field lines up to point B by fast-mode waves at their respective group velocities. Then an EIT wave front appears at footpoint C (as well as E). Subsequently, the deformation at point B is transferred down to footpoint D (as well as F) by Alfvén waves and up to the top of a higher field line by fast-mode waves with corresponding group velocities. Thus a new EIT wave front appears at footpoint D (as well as F). During the stretching process, the plasma on the outer side of the field line is compressed to form the density-enhanced EIT wave front, while inside the field line, the plasma is evacuated to form a dimming region due to the expansion.

Under the simplified assumption that all field lines are concentric semicircles, our model predicts that the apparent propagation velocity of EIT waves is $v_{\rm EIT} = {\rm CD}/\Delta t = 1/(v_f^{-1} + \frac{1}{2}\pi/v_{\rm A}^{-1}) \sim 0.34 v_f$ (where $v_{\rm A} = 0.8 v_f$ is assumed), that is, about 0.34 times the local fast-mode speed (Chen et al. 2002). It also implies that Moreton waves move about 3 or more times faster than EIT waves. In reality, field lines may be stretched in the solar radial direction as illustrated by the solid line GHI in Figure 8, which would greatly increase the transfer time from point B to points I through H and decrease the apparent propagation velocity of the EIT waves. When the field line GHI approaches infinity, as in the case of the interface between large-scale closed field lines and a coronal hole with open field lines, the transfer time would become infinite. It turns out that EIT waves stop near the boundary of a coronal hole. Therefore, our model not only can reconcile the velocity discrepancy between Moreton waves and EIT waves but also can explain why EIT waves avoid coronal holes. Besides, since EIT waves are generated by successive stretching of the field lines according to this model, it is also straightforward to understand why EIT waves are not seen around magnetic neutral lines. Based on our model, the EIT wave speed can be estimated for any given magnetic configuration. Figure 9 plots the theoretical motions of the EIT waves in case A (*left*) and case B (*right*) based on our model with the corresponding magnetic configurations shown in the two panels of Figure 1, that is, their initial distributions. The theoretical motions are qualitatively consistent with the simulation results displayed in the left panel of Figure 3 for case A and in Figure 7 for case B, respectively; for example, the EIT waves propagate continually outward in case A, while they are halted near the footpoint of the magnetic separatrix for case B; the averaged EIT wave speed for case A from $t = 4\tau_{\rm A}$ to $t = 10\tau_{\rm A}$ is estimated to be 128 ± 2 km s^{-1}, compared with 142 ± 4 km s^{-1} obtained from the numerical simulation. The deviation results from the deformation of the magnetic configuration after eruption.

4.2. *Relation to Moreton Waves*

According to our model, there should exist two types of coronal wave phenomena associated with a CME. A piston-driven shock wave straddles the CME, the legs of which are the

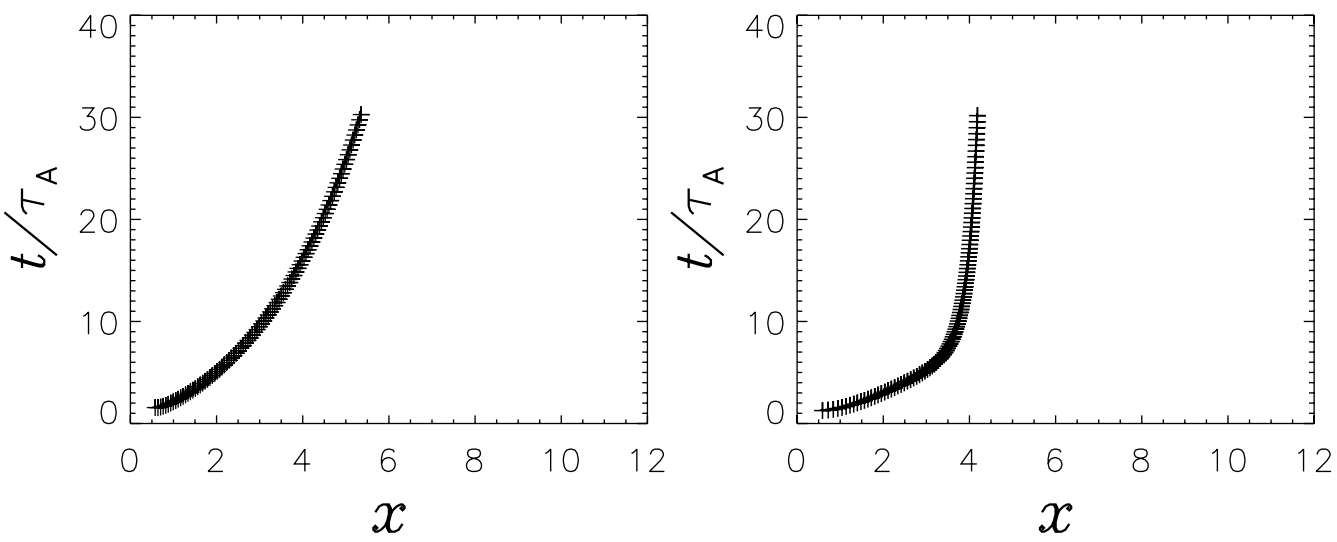

FIG. 9.—Theoretical estimate of the EIT wave motions in case A (*left*) and case B (*right*) based on our model sketched in Fig. 8. The corresponding magnetic configurations are shown in the two panels of Fig. 1.

coronal counterpart of the Hα Moreton waves. At the same time, a slower moving wave structure propagates outward with diffuse bright fronts followed by an expanding region of EUV dimming. The observed sharp EIT wave front, cospatial with Hα Moreton waves or SXR waves in some events, is just the coronal counterpart of the Hα Moreton wave front. Owing to the low time cadence of the *SOHO* EIT ($\sim$15 minutes), it is hardly possible to catch two coronal Moreton wave fronts if the coronal Moreton wave is moving very fast. However, in cases in which it moves with a low velocity, such as 300–400 km s^{-1}, it is still possible for the *SOHO* EIT to catch two or more EUV fronts cospatial with the Hα Moreton waves. This has been found for some events analyzed by Gilbert et al. (2004), Okamoto et al. (2004; the second event in their Table 1), Vršnak et al. (2002), and Warmuth et al. (2004a). The absence of a slower EIT wave in these events is probably due to weak wave fronts that are below the instrument's detection capability. With their high time cadence, EUV telescopes such as *TRACE* and the future *Solar-B* EUV Imaging Spectrometer will resolve two kinds of waves, that is, a fast-moving EUV wave with sharp fronts, followed by a slower moving "wave" with diffuse fronts. The fast-moving wave may have either bright or weak fronts, strongly depending on the temperature of the shocked plasma. Our model was strongly confirmed in an analysis combining *TRACE* and *SOHO* Coronal Diagnostic Spectrometer data by Harra & Sterling (2003), who presented the first high time cadence spectral observations of EIT waves. They found that a weak wave appears to emanate from a bright wave, with velocities of $\sim$500 and $\sim$200 km s^{-1}, respectively. The plasma between these two waves has a low Doppler velocity ($<$10 km s^{-1}). Combined with their earlier results about the strong Doppler motion inside the dimming region behind EIT waves (Harra & Sterling 2001), the whole picture is in good agreement with our model; that is, the fast-moving wave is the coronal counterpart of an Hα Moreton wave with very small Doppler motion in the downstream region, while the observed slow-moving EIT wave corresponds to a process of successive large-amplitude stretching of closed field lines with substantial Doppler motions inside. In this regard, we note in passing that both the horizontal and the vertical velocities, corresponding respectively to the Doppler motions in limb and disk events, are substantial only within the dimming region in our numerical results, though only the horizontal velocity was plotted in Chen et al. (2002).

Before the discovery of CMEs, Hα Moreton waves were though to be the sweeping skirts of flare-induced coronal fast-mode shock waves, which emit type II radio bursts (e.g., Uchida 1974). However, an investigation by Cliver et al. (1999) suggested that type II bursts, as well as Moreton waves, have their root cause in fast CMEs. This is consistent with our model, in which a piston-driven shock wave straddles the whole CME. This shock wave, as the source of type II radio bursts, may have been observed as SXR waves (e.g., Khan & Aurass 2002; Narukage et al. 2002; Hudson et al. 2003) and is also thought to be the acceleration region of CME-related nonthermal particles (Reames 1999; Aschwanden 2002). Bothmer et al. (1997) and Krucker et al. (1999) compared EIT wave positions and electron acceleration sites and found that the speed of the EIT waves is up to a factor of 2 too slow to propagate from the flare site to the footpoint of the Parker spiral connecting the Sun and the detecting spacecraft, along which energetic particles are transported. It was concluded that EIT waves are unlikely to be the source of the electron events. The results imply that the diffuse EIT waves are not cospatial with coronal Moreton waves, thereby providing indirect evidence to support our model. Quantitatively, the numerical results in Figure 4 indicate that the Mach number of the coronal Moreton wave decreases, with some fluctuations, to almost unity when the wave propagates to a large distance from the flare site. This could be consistent with the observational fact that Moreton waves are generally not detectable very far from the flare site (see Warmuth et al. 2004a). The figure also indicates that the Mach number of the type II bursts (top part of the piston-driven shock, which could also be observed as an SXR wave) is about 1.15–1.3, which is quite consistent with the values inferred from the observations by Hudson et al. (2003).

Pinter (1977) found that the estimated speeds of type II radio bursts exceeded, but were typically proportional to, the associated Moreton wave velocities. On the other hand, the statistical study by Klassen et al. (2000) indicated that the type II radio velocity and EIT wave speed are uncorrelated. The combined results, which are confirmed by our numerical results shown in Figure 5, further imply that Moreton waves and the general diffuse EIT waves are two distinct phenomena. The correlation between type II radio bursts and Moreton waves can be easily understood in our model, since they are considered to correspond to the top part and the leg of the same piston-driven shock, respectively. With a faster eruption of the flux rope, due to, say, a larger reconnection rate of the current sheet below, the Mach number of the piston-driven shock gets larger and the shock propagates faster. However, the so-called EIT waves in the general sense with diffuse fronts are not related to the shock wave; they are generated by successive stretching of the closed field lines covering the flux rope. Their apparent speed mainly depends on the magnetic field and the geometry.

It is interesting to find in the left panel of Figure 3 that about three ripples (a strong one and two intermediate ones) follow the outermost front of the coronal Moreton wave with the same velocity of travel, which can also be seen in Figure 2. They may explain the existence of two ripples in an SXR wave event discovered by Hudson et al. (2003). Analysis of the numerical results indicates that the ripples are generated during the acceleration of the driving source, that is, the flux rope. The process may be understood qualitatively as follows: After the flux rope is ejected, the perturbation propagates out, with the outermost front being the coronal Moreton wave; as the flux rope is accelerated, stronger piston-driven perturbations are formed traveling behind the outermost wave front at a super-Alfvénic speed.

4.3. *Stationary Fronts of EIT Waves*

The existence of a stationary front in some EIT wave events, lasting at least 17 minutes, presents a major challenge to the fast-mode wave explanation of the EIT wave phenomenon. Based on the result that stationary EIT fronts are cospatial with the footpoints of the separatrix between active regions, Delannée & Aulanier (1999) and Delannée (2000) proposed that EIT waves may be related to the opening of field lines and the stationary bright front may represent a compression of the plasma near the footpoints of the opening field lines located close to the separatrix. This is in accordance with the fact that EIT waves appear as almost circularly moving fronts when the photospheric magnetic field distribution is simple (e.g., if only one active region exists; see Fig. 2 of Thompson et al. 1998) and become dispersed or halt near the edge of the separatrix between active regions when the magnetic configuration on the Sun is complex (see Fig. 2 of Thompson et al. 1999). Case A in

this paper represents the situation in which the background magnetic structure is simple; in contrast, case B corresponds to the situation where other active regions are present in the background field. Note that the polarity of the pair of side active regions may have an orientation the same as or opposite to the source active region. In this paper, the polarity of the side active regions is opposite to that of the source active region. Our simulations reveal that in case A, the EIT wave propagates outward continually with a weak deceleration due to the decreasing, and more and more stretched, background magnetic field, as shown by Figure 3; in case B, however, the EIT wave decelerates outward until it reaches the boundary of another active region, where a separatrix is located. Thereafter, the EIT wave stops (near $x = 4.5$) to form a stationary front close to the magnetic separatrix, as indicated by both the numerical result (Fig. 7) and the analytical result (Fig. 9). This is similar to the 1999 June 13 event, in which an EIT wave propagated initially (Wills-Davey & Thompson 1999) and then stopped at a nearby separatrix (Delannée 2000).

This evolution in case B can be understood as follows: The magnetic configuration near the flux rope is slightly affected by the side active regions; therefore, the EIT waves initially propagate outward as in case A, with only the propagation velocity changed slightly. However, near the magnetic separatrix between the active regions, field lines are strongly convergent toward their footpoints near $x = 4.5$. According to our model sketched in Figure 8, the EIT waves become slower and slower as these field lines are being opened. Finally, when the field line closest to the separatrix is pushed to open, its leg keeps pressing the side active region to form a stationary front, since the field lines within the side active region are in another flux system and do not follow the stretching. In some other case in which the field lines near the separatrix are not convergent toward their footpoints, for example, if the side active regions have the same polarity orientation as the source active region, the EIT waves might not experience the strong deceleration process seen in the right panel of Figure 9. They may propagate to the separatrix with a substantial velocity and then be halted to form a stationary front, for the same reason as described above. Since the boundary of coronal holes is also a separatrix, it is not surprising that EIT waves are also observed to stop near them. At the same time, note that Figure 7 reveals that the EIT wave reappears beyond the active region near $x = 7.5$ after $t = 20\tau_A$, concurrent with the stationary wave front at $x = 4.3$, while the coronal Moreton wave propagates continually outward, although refracted by the active regions. From the discussion above, it may be concluded that EIT waves are not real waves; they are generated by the successive stretching of closed field lines, which is demonstrated by our model and has been suggested by Delannée & Aulanier (1999). Moreover, EIT waves would stop near a magnetic separatrix to form a stationary front, as demonstrated by both the numerical simulations (Fig. 7) and our analytic result (Fig. 9).

4.4. *Toward a Full View of EIT Waves*

The numerical simulations described in this paper, as well as those in Chen et al. (2002), demonstrate that, globally, there are two wave phenomena related to CME events. One is a fast-moving piston-driven shock wave that straddles the CME. Its upper part may be observed as a coronal SXR wave, which could also be the source of type II radio bursts. Its leg, that is, the coronal Moreton wave, sweeps the solar surface to form an Hα Moreton wave. Behind the coronal Moreton wave exists a slower moving wavelike structure with a density enhancement ahead of it. We propose that the propagating density enhancement near the solar surface corresponds to the observed "EIT wave," which results from the successive stretching of closed field lines. The mechanism underlying the EIT waves is schematically depicted by Figure 8. In our model, coronal Moreton waves are shock waves driven by CMEs, while EIT waves correspond to the successive stretching of field lines covering the erupting flux rope rather than to real waves.

According to our model, the wave phenomena associated with CMEs may present the following characteristics:

1. There should be two types of wave phenomena in the corona during an eruption, where the fast-moving wave is the coronal counterpart of the Hα Moreton wave (or the coronal Moreton wave), while the slower moving one is the EIT wave, with diffuse fronts.
2. If only a single active region exists on the solar surface as in case A of this paper, the EIT wave propagates continually; in contrast, when another active region is present in the background magnetic field, the propagating EIT wave will stop near the separatrix between the two active regions.
3. Owing to its low time cadence, *SOHO*'s EIT may catch several "EIT wave" fronts and at most one front of the coronal Moreton wave in one event if the coronal Moreton wave is moving very fast. Several EUV fronts cospatial with Hα Moreton waves can be captured only if the coronal Moreton waves have velocities near the lower limit, say, 300–400 km s^{-1}. In this case, the much slower EIT wave fronts are often too weak to be detected.
4. The observed EIT wave speeds depend on both the magnetic field strength and the magnetic geometry. Theoretical analysis indicates that if the field lines covering the flux rope are close to a dipole field with concentric semicircular field lines, the EIT wave speeds will be about one-third of the local coronal Moreton wave speeds near the solar surface; if the field lines are strongly stretched in the solar radial direction, as probably occurs near the boundary of active regions, the EIT wave speeds would be much smaller than that of the local coronal Moreton waves near the solar surface. Therefore, it could be possible for the EIT wave speed to be higher in the quiet regions than near active regions, as found by Foley et al. (2003). A simulation of this is reserved for a separate paper.
5. With the assumption that the upper part of the piston-driven shock is the source of type II radio bursts, our simulations indicate that the propagation velocities of type II radio bursts are larger than, and nearly proportional to, those of Moreton waves, while being almost uncorrelated with those of EIT waves, a result comparable to observations.
6. The "EIT dimming" phenomenon should be closely associated with EIT waves, since an expanding plasma-depleted region with strong Doppler motions is left behind an EIT wave, while there are no substantial Doppler motions between the coronal Moreton wave and the EIT wave.

The research by Biesecker et al. (2002) indicates that if an EIT wave is observed, then there must be a CME. This is consistent with our model in which EIT waves are generated by successive stretching (or opening) of closed field lines, which is widely believed to be involved in CMEs. However, they also pointed out that not all CMEs have associated EIT waves, though field-line opening occurs in all CMEs. Kay et al. (2003) further show that the occurrence of EIT waves among CME events is not correlated with the speed of the CME. It thus becomes a

question why EIT waves are absent in some CME events. Besides the role of the background magnetic configuration, we postulate that the Fe XII 195 Å signature of the EIT waves during a CME event strongly depends on the initial temperature of the plasma, since our numerical results indicate that the plasma temperature increases weakly inside the EIT wave fronts, while the contribution function of the emission line is very sensitive to the temperature. To make a more detailed comparison between numerical simulations and observations, Fe XII 195 Å images should be synthesized on the basis of MHD numerical results, a task to which we will devote a future paper.

The authors thank an anonymous referee for many constructive suggestions. The research is supported by grants from the Chinese foundations FANEDD (200226), NSFC (10221001, 10333040, and 10403003) and NKBRSF (G20000784).

REFERENCES

Aschwanden, M. J. 2002, Space Sci. Rev., 101, 1
Biesecker, D. A., Myers, D. C., Thompson, B. J., Hammer, D. M., & Vourlidas, A. 2002, ApJ, 569, 1009
Bothmer, V., et al. 1997, in Proc. 31st ESLAB Symp., Correlated Phenomena at the Sun, in the Heliosphere and in Geospace, ed. A. Wilson (ESA SP-415) (Noordwijk: ESA), 207
Chen, P., Fang, C., & Hu, Y. 2000, Chinese Sci. Bull., 45, 798
Chen, P. F., & Shibata, K. 2000, ApJ, 545, 524
Chen, P. F., Wu, S. T., Shibata, K., & Fang, C. 2002, ApJ, 572, L99
Cliver, E. W., Webb, D. F., & Howard, R. A. 1999, Sol. Phys., 187, 89
Delaboudinière, J.-P., et al. 1995, Sol. Phys., 162, 291
Delannée, C. 2000, ApJ, 545, 512
Delannée, C., & Aulanier, G. 1999, Sol. Phys., 190, 107
Dere, K. P., et al. 1997, Sol. Phys., 175, 601
Eto, S., et al. 2002, PASJ, 54, 481
Foley, C. R., Harra, L. K., Matthews, S. A., Culhane, J. L., & Kitai, R. 2003, A&A, 399, 749
Forbes, T. G. 1990, J. Geophys. Res., 95, 11919
Gilbert, H. R., Holzer, T. E., Thompson, B. J., & Burkepile, J. T. 2004, ApJ, 607, 540
Harra, L. K., & Sterling, A. C. 2001, ApJ, 561, L215
———. 2003, ApJ, 587, 429
Hu, Y.-Q. 1989, J. Comput. Phys., 84, 441
Hudson, H. S., Khan, J. I., Lemen, J. R., Nitta, N. V., & Uchida, Y. 2003, Sol. Phys., 212, 121
Kai, K. 1970, Sol. Phys., 11, 310
Kay, H. R. M., Harra, L. K., Matthews, S. A., Culhane, J. L., & Green, L. M. 2003, A&A, 400, 779
Khan, J. I., & Aurass, H. 2002, A&A, 383, 1018
Klassen, A., Aurass, H., Mann, G., & Thompson, B. J. 2000, A&AS, 141, 357
Krucker, S., Larson, D. E., Lin, R. P., & Thompson, B. J. 1999, ApJ, 519, 864
Lin, J. 2004, Sol. Phys., 219, 169
Lin, J., & Forbes, T. G. 2000, J. Geophys. Res., 105, 2375
Moreton, G. E., & Ramsey, H. E. 1960, PASP, 72, 357
Moses, D., et al. 1997, Sol. Phys., 175, 571
Narukage, N., Hudson, H. S., Morimoto, T., Akiyama, S., Kitai, R., Kurokawa, H., & Shibata, K. 2002, ApJ, 572, L109
Okamoto, T. J., Nakai, H., Keiyama, A., Narukage, N., Ueno, S., Kitai, R., Kurokawa, H., & Shibata, K. 2004, ApJ, 608, 1124
Pinter, S. 1977, in Contributed Papers to the Study of Travelling Interplanetary Phenomena/1977, ed. M. A. Shea, D. F. Smart, & S.-T. Wu (Spec. Rep. AFGL-SR-209) (Hanscom AFB: Air Force Geophys. Lab.), 35
Reames, D. V. 1999, Space Sci. Rev., 90, 413
Smith, S. F., & Harvey, K. L. 1971, in Physics of the Solar Corona, ed. C. J. Macris (Dordrecht: Reidel), 156
Thompson, B. J., Plunkett, S. P., Gurman, J. B., Newmark, J. S., St. Cyr, O. C., & Michels, D. J. 1998, Geophys. Res. Lett., 25, 2465
Thompson, B. J., Reynolds, B., Aurass, H., Gopalswamy, N., Gurman, J. B., Hudson, H. S., Martin, S. F., & St. Cyr, O. C. 2000, Sol. Phys., 193, 161
Thompson, B. J., et al. 1999, ApJ, 517, L151
Uchida, Y. 1968, Sol. Phys., 4, 30
———. 1974, Sol. Phys., 39, 431
Vršnak, B., Warmuth, A., Brajša, R., & Hanslmeier, A. 2002, A&A, 394, 299
Wang, Y.-M. 2000, ApJ, 543, L89
Warmuth, A., Vršnak, B., Aurass, H., & Hanslmeier, A. 2001, ApJ, 560, L105
Warmuth, A., Vršnak, B., Magdalenić, J., Hanslmeier, A., & Otruba, W. 2004a, A&A, 418, 1101
———. 2004b, A&A, 418, 1117
Wild, J. P., Smerd, S. F., & Weiss, A. A. 1963, ARA&A, 1, 291
Wills-Davey, M. J., & Thompson, B. J. 1999, Sol. Phys., 190, 467
Wu, S.-T., Zheng, H., Wang, S., Thompson, B. J., Plunkett, S. P., Zhao, X.-P., & Dryer, M. 2001, J. Geophys. Res., 106, 25089